2026 IEEE International Conference on Robotics and Automation (ICRA 2026)
June 1-5, 2026. Vienna, Austria

A Manta Ray Robot with Tunable Two-Dimensional Wing Stiffness

Sicheng Fu[1], and Wei Wang[1,*]

Abstract— **Manta rays achieve efficient, highly maneuverable three-dimensional swimming by flapping their large pectoral fins in both the spanwise and chordwise directions, where fin stiffness likely plays a critical role in hydrodynamic performance. However, most existing manta-ray robots use fixed or one-dimensional compliance, which limits their ability to reproduce the two-dimensional stiffness variations necessary for authentic 3D traveling-wave propulsion. This paper presents a bioinspired manta ray robot equipped with an active stiffness control mechanism that enables tunable two-dimensional stiffness in its pectoral fins. The design integrates a cable-driven actuation system with anisotropic disks, providing multiple distinct stiffness in both the spanwise and chordwise directions that can be locked during operation. Mechanical characterization confirms periodic stiffness variation, with spanwise stiffness increasing by more than 30% and chordwise stiffness decreasing by about 10% as the disk rotates from 0° to 90°, then recovering from 90° to 180°. Thrust tests demonstrate that stiffness substantially affects steady-state thrust; under certain conditions, the optimal setting produces up to five times more thrust than the least effective one. Free-swimming trials further reveal that stiffness alters swimming speed, with up to 20% variation observed in low-frequency, large-amplitude flapping. These results highlight the potential of active stiffness control to enhance the performance of bio-inspired underwater robots and provide new insights into the role of structural compliance in aquatic locomotion.**

I. Introduction

Bio-inspired locomotion has become a powerful paradigm for advancing autonomous underwater vehicle (AUV) technology [1]–[3]. Robotic platforms inspired by diverse marine species, including eel-like robots [4], [5], carangiform and anguilliform fish robots [6], [7], jellyfish-like robots [8], [9], have demonstrated improved maneuverability, efficiency, and environmental adaptability compared to traditional propeller-driven designs. Among these, manta rays and their relatives employ Mobuliform swimming, a propulsion mode driven by the oscillation of two broad pectoral fins [10]. In nature, manta rays achieve high speeds, exceptional agility, and remarkable energy efficiency during behaviors such as migration, foraging, and predator avoidance, all while maintaining smooth, stable body trajectories [11]. These characteristics make ray-inspired robots particularly promising templates for next-generation AUVs intended for maritime services, long-range exploration, and complex underwater missions [12].

Although numerous bioinspired aquatic robots have been proposed and demonstrated [13], [14], their swimming performance still lags significantly behind that of their natural counterparts. Bridging this gap remains a central challenge in bio-inspired robotics. A prevailing approach has been to transition robotic fish from rigid to flexible structures, leading to the development of numerous soft aquatic robots over the past one to two decades [15], [16].

Fin stiffness has been identified as a critical factor influencing bio-inspired aquatic locomotion [17], [18]. Building on this insight, recent efforts have explored variable-stiffness mechanisms to further enhance efficiency and adaptability in flexible robotic fish [19], employing approaches such as tunable joints, granular jamming, and smart materials [19]–[21]. Although direct evidence of active stiffness modulation in manta rays is not yet available, multiple indirect observations suggest its biological relevance. Comparative studies between ray species show systematic variation in fin stiffness with body size and habitat [22], [23]. Stingray investigations, which are a closely related group with similar morphology but a distinct swimming mode, demonstrate that they actively modulate body stiffness through muscle activation to adapt to different swimming speeds [24]. These findings strongly suggest that manta rays may also employ active stiffness control, which could provide substantial benefits for locomotor efficiency and adaptability.

Numerous ray-inspired robotic platforms have been developed in recent years [25], advancing ray-mimetic design and clarifying how ray-like locomotion can improve swimming performance. However, most manta-ray robots still use multi-joint pectoral fins [26], [27], which provide articulated motion but limited intrinsic compliance, or fixed-stiffness fins [28], [29]. Only a few designs incorporate adjustable stiffness in the literature. For example, Xiang et al. [21] integrated an adjustable-stiffness band that produced distinct thrust and speed profiles across settings, and related work [20] employed an elastic deformable structure to vary fin stiffness. Despite these advances, existing ray-inspired and fish-like robots generally realize only one-dimensional stiffness variation. However, manta rays achieve three-dimensional (3D) swimming by flapping their large pectoral fins in both the spanwise and chordwise directions. This 3D motion of pectoral fins that likely relies on two-dimensional stiffness variations to produce authentic 3D traveling-wave propulsion [12].

Building on this motivation, we present a manta ray–inspired robot featuring a novel adjustable-stiffness mechanism that enables two-dimensional (spanwise and chordwise) stiffness variation, overcoming the limitations of prior designs restricted to fixed or one-dimensional compliance. This tunable two-dimensional wing stiffness platform serves as an effective testbed for studying active stiffness control in three-dimensional fin propulsion for bio-inspired

[1]Marine Robotics Lab, Department of Mechanical Engineering, University of Wisconsin–Madison, Madison, WI 53706, USA.
[*]Corresponding author: Wei Wang (e-mail: wwang745@wisc.edu).

locomotion. The key contributions of this work are summarized as follows:

- A manta ray–inspired robotic platform equipped with an actively adjustable mechanism that enables two-dimensional stiffness variation.
- Mechanical characterization confirming direction-dependent stiffness states and quantifying the achievable stiffness range.
- Experimental study investigating the impact of fin stiffness on fin motion, thrust output, and swimming performance.

II. Robot Design

To investigate adjustable-stiffness propulsion, we developed a manta ray–inspired robotic platform designed for three-dimensional swimming studies. The following section details the prototype's structural design, electronics, and actuation systems that enable independent fin flapping and stiffness control.

A. Prototype Design

The prototype measures 400 mm in body length (head to tail) and 600 mm in fin span (tip to tip). Its principal components include a waterproof enclosure, 30 mm thick and 160 mm wide, which houses all onboard electronics and the battery pack. A pair of pectoral fins, each 5 mm thick and 200 mm wide, are equipped with adjustable-stiffness mechanisms actuated by two front-mounted servos. Two rear-mounted servos drive a cable-based stiffness adjustment system. A stabilizing tail provides directional stability, while a structural frame connects and supports all modules.

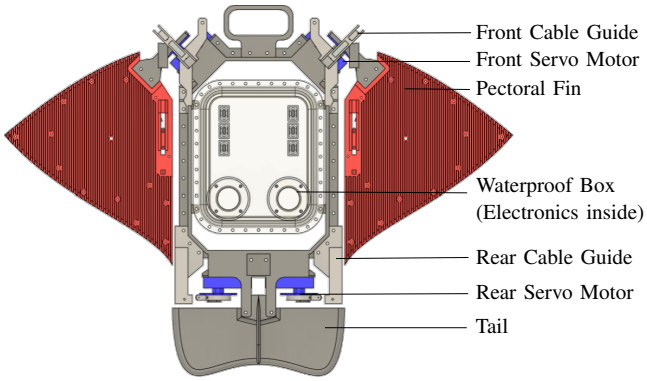

(a)

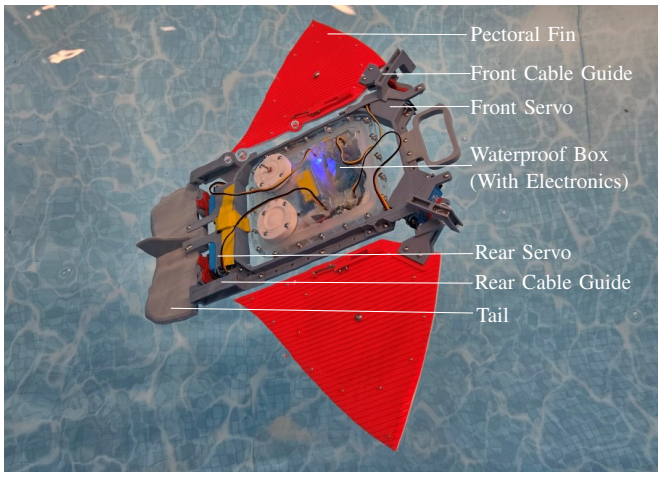

(b)

Fig. 1. Manta ray robot prototype. (a) CAD model showing major components, including pectoral fins, tail, waterproof box, front and rear servos, and cable guides. (b) Photograph of the robot during swimming.

The waterproof enclosure is fabricated using FormLab ClearV5 resin to improve resistance to leakage. All access points are sealed with a silicone O-ring and two custom-molded silicone caps (Smooth-On rubber), which protect the main electronics access port, the charging interface, and the power switch feedthrough. Details regarding the pectoral fin fabrication process are provided in subsequent sections. All other structural components are 3D-printed using BambuLab PLA.

To minimize external interference during swimming tests, the robot operates fully untethered, carrying all necessary electronics onboard and receiving commands wirelessly. As autonomy is not the primary focus at this stage, the robot is controlled in an open-loop configuration: no sensors are integrated, actuators are driven directly through remote commands, and buoyancy is manually adjusted to maintain neutral stability. A CAD rendering and a photograph of the prototype are shown in Fig. 1.

B. Electronics

The robot is powered by a two-cell 7.4 V Li-Po battery pack. The four servo motors are supplied directly from the battery output, while a DC–DC converter regulates the voltage to provide 5 V and 3.3 V rails for the remaining electronic components. An STM32F303C8T6 microcontroller (MCU) processes incoming commands and generates control signals for the servos. Each servo is actuated using an independent PWM waveform, as described in detail in the following subsection. Wireless communication is achieved using a pair of ESP8266 Wi-Fi modules: one connected to the MCU via a UART interface onboard the robot and the other connected to a laptop through USB. This configuration enables command transmission from a custom laptop interface to the robot. Because Wi-Fi signals attenuate rapidly underwater, commands are uploaded either prior to deployment or after retrieval.

C. Actuation

Four HiTEC HS-646WP waterproof servo motors are employed, each providing a motion range of $\pm 60^\circ$, a maximum speed of 60° in 0.17 s, a stall torque of 11.6 kg·cm, and supporting 40 Hz control input. The two front-mounted servos actuate the pectoral fins. They are positioned such that their output shafts lie within the robot's mid-plane and are oriented 45° relative to the body midline, enabling effective flapping motion.

The commanded trajectory of the front servo angle, $Q(t)$, follows a sinusoidal profile:

$$Q(t) = A\sin\left(\tfrac{2\pi}{T}t + B\right) + C,$$

where t is elapsed time, A is the amplitude (limited to $A < 60^\circ$ by the servo), T is the period, B is the phase, and C is the angular offset. All parameters are independently programmable for the left and right fins. In the experiments reported here, only A and T were varied (identically for both fins), while B and C were fixed at zero, resulting in symmetric flapping without phase difference or angular offset. Future work on maneuverability and stabilization may exploit nonzero phase or offset values.

The two rear servos actuate the cable-driven stiffness-adjustment mechanism. A scroll attached to each servo winds or releases a cable routed through a series of guides to a slider embedded in the pectoral fin. The cable path is designed to minimize unintended tension from fin flapping, ensuring that only the rear servos influence the stiffness mechanism.

III. Adjustable-Stiffness Pectoral Fin Design

Inspired by anisotropic bending behavior, we develop a 2D adjustable stiffness mechanism. This section explains how combining plates with direction-dependent stiffness can produce controllable stiffness distributions for the manta ray robot's fins.

A. Adjustable Stiffness Principle

First, we introduce the principle of achieving variable stiffness by arranging plates with anisotropic bending properties, i.e., plates whose stiffness varies depending on the bending orientation at specific relative angles. Consider a disk with anisotropic stiffness, such as one containing parallel thickened stripes. As illustrated in Fig. 2a, the disk is most compliant when bent along a preferred orientation, stiffest when bent perpendicularly, and exhibits intermediate stiffness values at other orientations. The bending stiffness is characterized by the product of Young's modulus and the second moment of area, EI, which may be expressed as a function $EI(\theta)$ of the bending orientation θ. When two such disks are combined as shown in Fig. 2b, sharing identical bending displacements and force outputs, the total stiffness is the sum of their individual contributions:

$$EI_{\text{total}}(\theta) = EI_{\text{top}}(\theta - \theta_{\text{top}}) + EI_{\text{bottom}}(\theta - \theta_{\text{bottom}}),$$

where θ is the bending torque orientation in the world frame, θ_{top} is the orientation of the top disk in the world frame, and θ_{bottom} is the orientation of the bottom disk in the world frame, as shown in Figure 2b. By varying the relative angle between the two disks, $\theta_{\text{top}} - \theta_{\text{bottom}}$, the overall stiffness distribution can be tuned, as demonstrated in Fig. 2b.

If the top and bottom disks are oriented at fixed angles θ_{top0} and θ_{bottom0} in the world frame, their orientations become $\theta_{\text{top}} = \theta + \theta_{\text{top0}}$ and $\theta_{\text{bottom}} = \theta + \theta_{\text{bottom0}}$. The total stiffness can then be rewritten as:

$$EI_{\text{total}}(\theta) = EI_{\text{top}}(\theta + \theta_{\text{top0}}) + EI_{\text{bottom}}(\theta + \theta_{\text{bottom0}}).$$

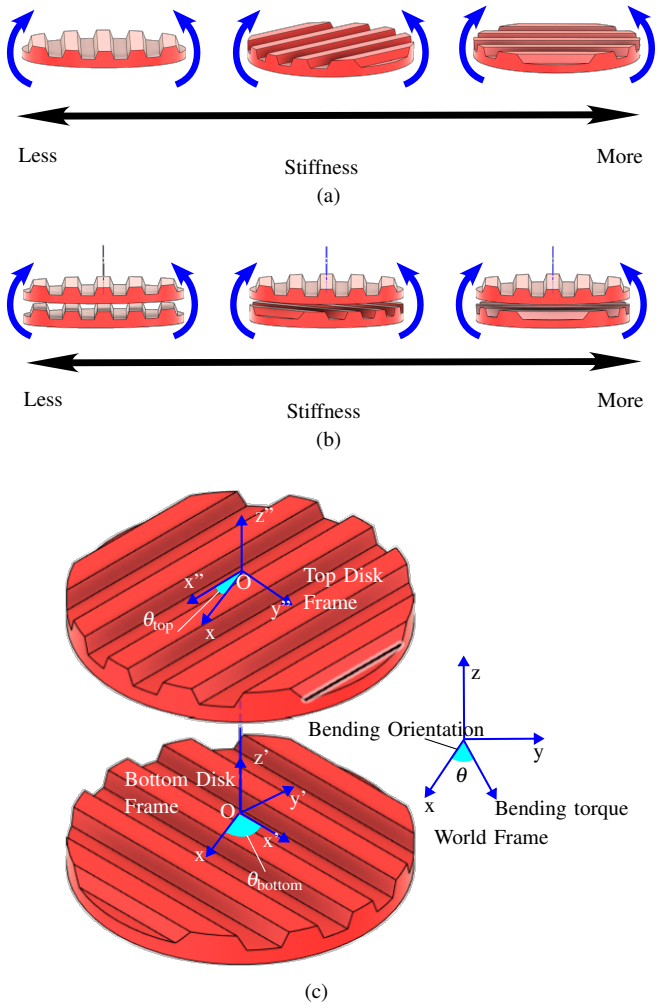

Fig. 2. Principle of adjustable stiffness based on anisotropic disks. (a) A single anisotropic disk exhibits direction-dependent compliance: it is most flexible along one orientation, stiffest along the perpendicular, and intermediate in between. (b) When two disks are combined, the overall stiffness distribution varies with their relative angle, producing tunable stiffness patterns. (c) The coordinate system definition. World Frame, Top Disk Frame (fixed to top disk) and Bottom Disk Frame (fixed to bottom disk) share the same origin while having different orientation.

B. Geometry & Fabrication

The adjustable-stiffness pectoral fin design is illustrated in Fig. 3. For structural integration, one disk is fixed relative to the robot body and extended to form the fin's *top layer*. A softer *bottom layer* is attached beneath it. A second disk is sandwiched between the two layers to enable bending displacement and torque transfer; this disk is referred to simply as the *disk*. The disk can rotate continuously through 360° and lock into 24 equally spaced positions (15° increments). In this design, the origin is defined at the center of the pectoral fin. The world frame has such orientation: x axis points to head, y axis points to left, z axis points to top. The Top Layer Frame is fixed to top layer, which means it always has the same orientation as the world frame and $\theta_{\text{top}} = 0$. The Disk Frame is fixed to the disk, which means it has an z-rotattion angle, called as Disk Angle in later sections, ϕ to the world frme and $\theta_{\text{bottom}} = \phi$. The

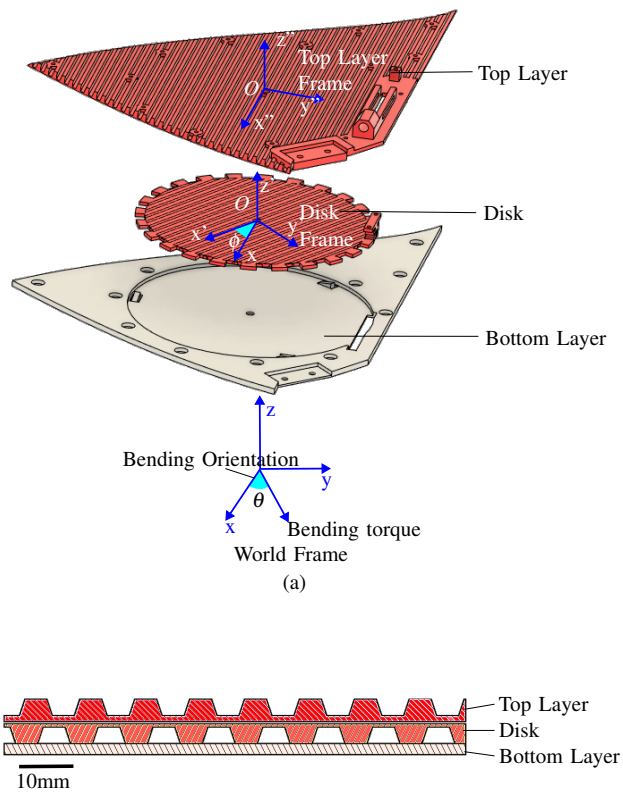

Fig. 3. Adjustable-stiffness pectoral fin. (a) Overview of the three main components: top layer, disk, and bottom layer. (b) Section view of the fin assembly, showing the thickness of each part and the dimensions of the stripes.

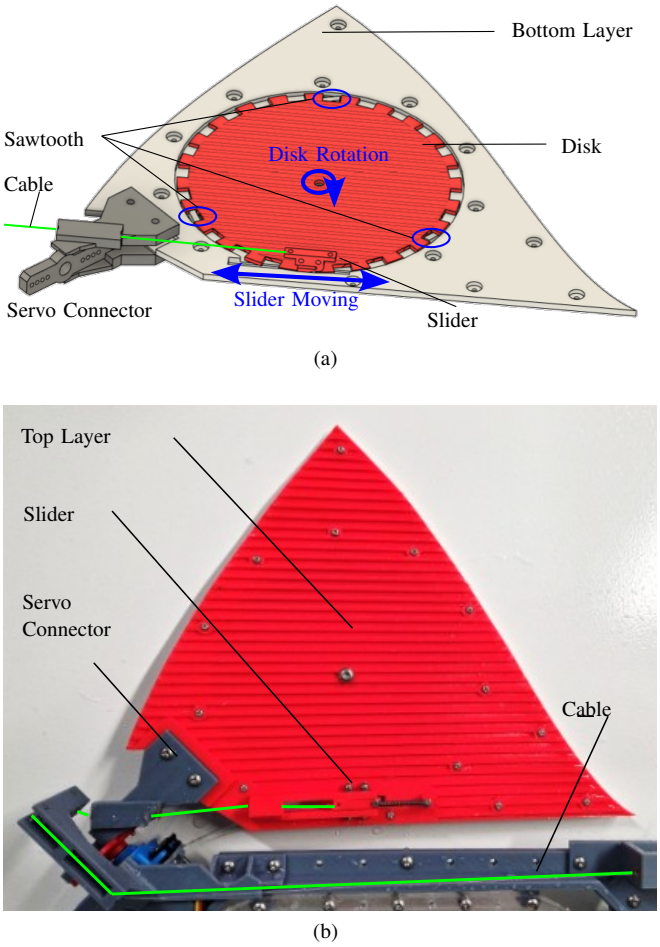

Fig. 4. Cable-driven adjustable-stiffness mechanism. (a) Mechanical design, with the top layer hidden to show essential components: the disk with 24 protrusions, the bottom layer with sawtooth features preventing backward rotation, and the slider driven by the cable system. (b) Photograph of the fabricated pectoral fin, showing the slider motion direction and disk rotation direction.

Stripes of 5.0 mm width are evenly distributed on both the top layer and the disk, with alternating thick (2.0 mm) and thin (0.5 mm) segments to provide anisotropic stiffness. The top layer and disk are fabricated using BambuLab TPU for AMS, while the bottom layer is printed with TPU90A. For 3D printing, the top layer and the disk is produced with a layer thickness of 0.08 mm and a 100% infill ratio, whereas the bottom layer is printed with a layer thickness of 0.16 mm and a 15% infill ratio.

C. Mechanism

The cable-driven mechanism provides active adjustment of fin stiffness by rotating the middle disk and locking it into discrete positions. As shown in Fig. 4, the disk incorporates 24 evenly spaced protrusions distributed around its circumference. A sawtooth-shaped slider, attached to a cable, engages these protrusions. The slider is fabricated from soft TPU95A, allowing it to push against the protrusions during forward motion while flexing to slide over them during the return stroke.

When the cable is pulled by a rear-mounted servo, the slider advances, rotating the disk forward by a single 15° step. A restoring extension spring repositions the slider during its return stroke. To prevent reverse rotation and maintain the current stiffness setting, additional sawtooth features are fixed to the bottom fin layer. Each actuation cycle advances the disk by one increment, enabling full 360° rotation through all 24 positions.

IV. Robot Tests and Results

This section details the experimental evaluation of the robot. First, the stiffness characteristics of the adjustable-stiffness pectoral fin are quantified. Subsequently, three categories of robot-level experiments are performed to systematically assess the influence of fin stiffness on swimming performance.

A. Two-Dimensional Stiffness Characterization

This subsection characterizes the two-dimensional stiffness properties of the pectoral fin and evaluates how the adjustable-stiffness mechanism influences its stiffness distribution. A simplified prototype fin—fabricated without the active rotation mechanism and manually adjusted for disk settings—was used for testing. The fin was mounted on an Instron testing machine using a custom clamp, as shown in

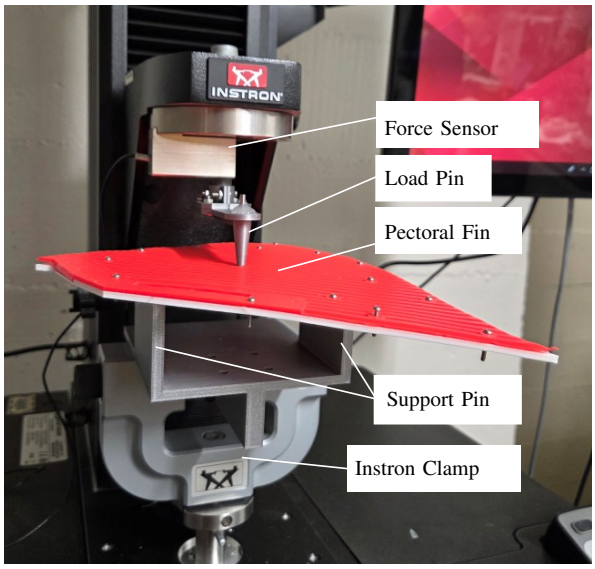

(a)

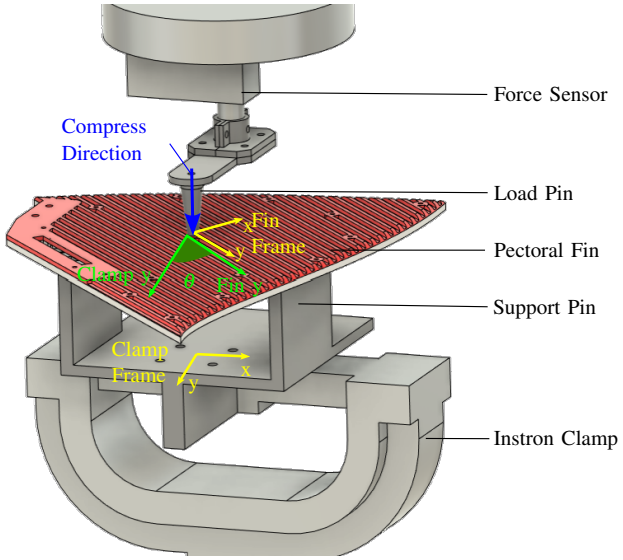

(b)

Fig. 5. Stiffness characterization setup. (a) Photograph of the clamp and pectoral fin mounted on the Instron machine. (b) Schematic of the bending test, defining the orientation angle θ between the y-axis of the clamp frame and the y-axis of the fin frame. During the test, the load pin moves downward (blue arrow), while force and displacement in that direction are recorded.

Fig. 5, and a standard three-point bending test was performed to measure stiffness at various orientations.

During testing, the Instron machine gradually displaced a force sensor downward, causing its attached load pin to press on the fin's center. The corresponding displacement and force values were recorded for subsequent analysis. Five orientations ($\theta = 0°, 22.5°, 45°, 67.5°, 90°$) were tested for each of the 24 disk positions ($\phi = 15n°$, $n = 0, 1, \ldots, 23$). Each measurement was repeated twice, and the mean values were used for analysis.

For each orientation, bending stiffness $EI(\theta)$ was calculated as

$$EI(\theta) = \frac{FL^3}{48\delta},$$

where F is the measured force, δ is the corresponding displacement, and L is the distance between support pins (100 mm in this setup). The resulting $EI(\theta)$ curves for all disk positions are presented in Fig. 6.

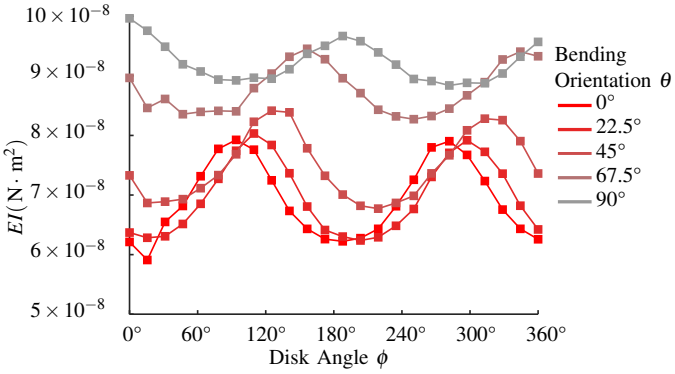

Fig. 6. Pectoral fin stiffness variation. As the disk rotates ($\phi = 0°$ to 360°), the bending stiffness EI is measured at five orientations: $\theta = 0°, 22.5°, 45°, 67.5°, 90°$. The curves demonstrate direction-dependent stiffness changes, with the largest variation in spanwise direction($\theta = 0°$) and the smallest in chordwise direction($\theta = 90°$).

The measurements reveal that stiffness varies across all orientations as the disk rotates. Along the spanwise direction ($\theta = 0°$), stiffness exhibits the largest variation, ranging from approximately $6 \times 10^{-8}\,\mathrm{N \cdot m^2}$ to $8 \times 10^{-8}\,\mathrm{N \cdot m^2}$. In contrast, along the body-length direction ($\theta = 90°$), stiffness varies less significantly, with values between 9×10^{-8} and $10 \times 10^{-8}\,\mathrm{N \cdot m^2}$. The stiffness curves repeat every 180° (12 positions), consistent with the geometric symmetry of the disk, and exhibit a phase lag of approximately one-quarter period as θ increases from 0° to 90°.

Overall, the mechanism achieves seven distinct stiffness levels corresponding to disk settings $\phi = 0°, 15°, 30°, 45°, 60°, 75°, 90°$. Among these, $\phi = 0°$ produces the lowest stiffness, whereas $\phi = 90°$ yields the highest. These findings confirm that the fin's stiffness distribution can be tuned systematically, suggesting potential implications for optimizing flapping kinematics and swimming performance.

Based on these findings, We can use the following formula to analog the stiffness distribution:

$$EI(\theta, \phi) = A(\theta) cos(2\phi + 2\theta) + B(\theta)$$

Where $A(\theta) = A_1 sin(\theta) + A_2$, $A_1 = 7.6561 \times 10^{-9}$, $A_2 = -5.9625 \times 10^{-9}$; $B(\theta) = B_1 cos(\theta) + B_2$, $B_1 = -2.5263 \times 10^{-8}$, $B_2 = 9.3960 \times 10^{-8}$.

B. Fin Kinematics Analysis

Fin kinematics were analyzed by recording the steady-state motion of the pectoral fin. The robot was secured to a rigid frame and filmed using a GoPro Hero 9 camera positioned on the side. Video was captured at 4K resolution and 30 fps.

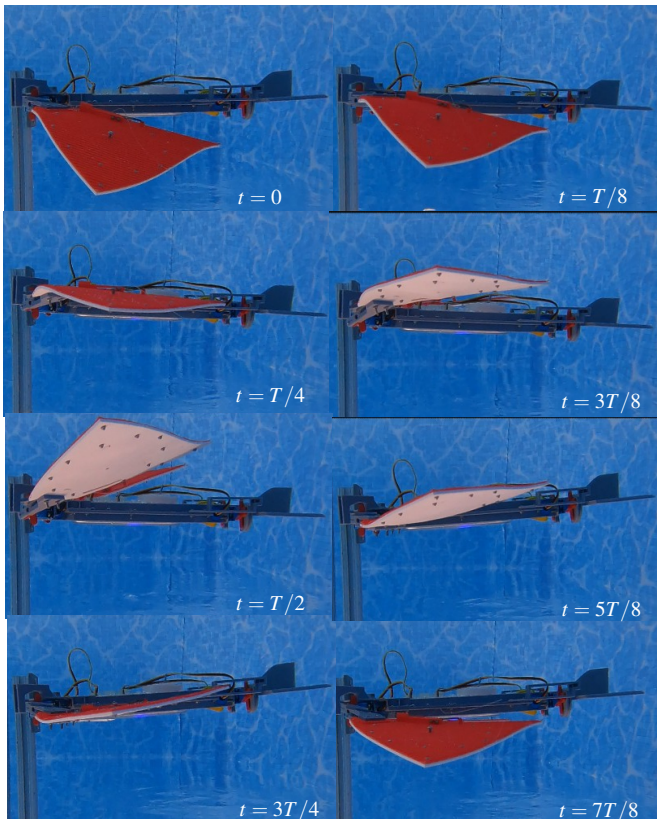

(a)

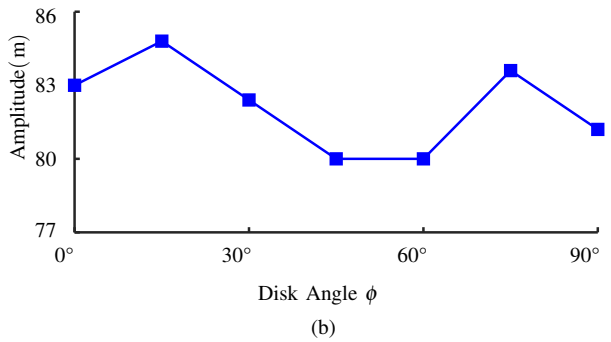

(b)

Fig. 7. Fin kinematics filming. (a) A flapping cycle of the pectoral fin (b) Tip amplitude measured under different stiffness settings, showing a non-monotonic variation as the disk setting ϕ changes from 0° to 90°.

From the recordings, the fin outline was traced, and the tip displacement amplitude was extracted for comparison. During testing, the robot's pectoral fins were actuated at a frequency of 0.667 Hz with a flapping amplitude of 30°. One typical fin flapping cycyle under this flapping setting is shown in Figure.7a. The definition of tip displacement amplitude is the maximum distance of the fin tip from its initial position, and measured amplitudes for different disk settings are presented in Figure. 7b.

The results indicate that tip displacement amplitude varies between 0.160 m and 0.168 m as ϕ changes from 0° to 90°. The relationship is non-monotonic: the amplitude initially decreases before increasing again. This trend demonstrates that fin stiffness directly affects flapping kinematics. The impact of these kinematic variations on swimming performance will be examined in subsequent sections.

C. Thrust Test Evaluation

The thrust test was conducted to evaluate the steady-state thrust force generated by the robot. As shown in Fig. 8a, the robot was mounted on a fixed supporting frame, and forward thrust was measured using an ATI force sensor. Data were recorded in real time at approximately 60 Hz. A baseline reading was first obtained with the robot positioned but inactive, and this static offset was subtracted from subsequent measurements. Because thrust acts along the negative z-axis of the sensor frame, the z-component of the measured force was used directly as the thrust value. Time–thrust curves were plotted to capture temporal variations, and the mean thrust over more than ten flapping cycles ($N > 10$) was calculated to enable quantitative comparison across stiffness settings.

Two actuation conditions were tested: (i) low-frequency, large-amplitude flapping (0.667 Hz, 30° amplitude) and (ii) high-frequency, small-amplitude flapping (3 Hz, 12° amplitude). Seven stiffness configurations were examined by adjusting the disk angle ϕ ($0°, 15°, 30°, 45°, 60°, 75°, 90°$). Representative thrust measurements are shown in Figure. 8.

The results demonstrate that stiffness exerts a strong influence on thrust generation, with trends dependent on the flapping regime. For low-frequency, large-amplitude flapping, thrust initially decreases before increasing as ϕ increases from 0° to 90°. The maximum thrust of 0.565 N occurs at $\phi = 90°$, nearly five times greater than the minimum observed at $\phi = 30°$. Under high-frequency, small-amplitude conditions, thrust first increases, reaching a maximum of 0.0745 N at $\phi = 60°$, and then decreases at larger angles.

Overall, these measurements highlight the critical role of fin stiffness in propulsive performance. The non-monotonic trends—decrease then increase at low frequency, increase then decrease at high frequency—indicate that optimal stiffness is regime-dependent, supporting the hypothesis that fin–fluid interactions are highly sensitive to structural compliance.

D. Free-Swimming Test Evaluation

The free-swimming test was conducted to evaluate the influence of fin stiffness on swimming speed. As shown in Fig. 9(a), the robot swam freely in a pool while being recorded by an overhead camera. The pool measured approximately 5 m in length, 2.5 m in width, and 1 m in depth. A GoPro Hero13 camera, mounted on the ceiling approximately 2 m above the water surface and set to Wide mode, captured the trials. Although the camera's field of view encompassed only part of the pool, image distortion was minimal, making it suitable for accurately tracking the robot. Video was recorded at 4K resolution and 30 fps, and the robot's position over time was extracted to estimate its average swimming speed.

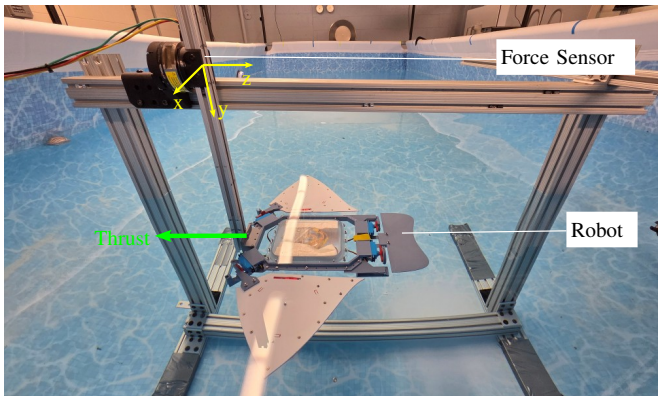

(a)

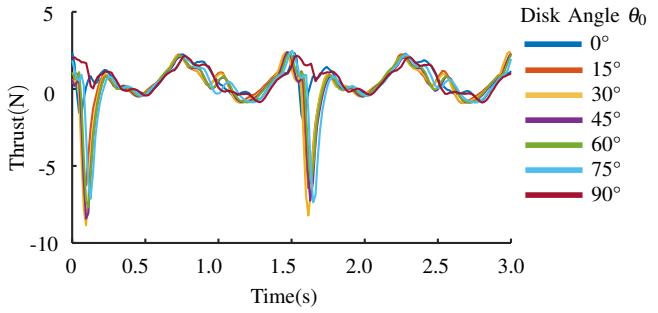

(b)

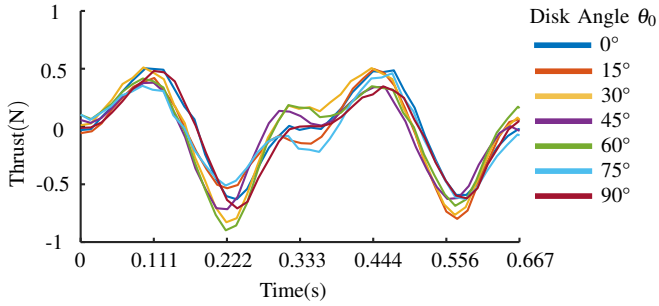

(c)

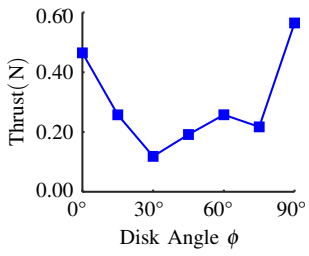

(d)

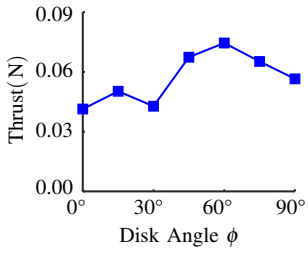

(e)

Fig. 8. Thrust test results. (a) Experimental setup showing the robot mounted on a frame with an ATI force sensor. (b) Time-Thrust curve for underwater flapping at 0.667 Hz and 30° amplitude (c) Time-Thrust curve for flapping at 3 Hz and 12° amplitude (d) Average thrust for underwater flapping at 0.667 Hz and 30° amplitude. (e) Average thrust for underwater flapping at 3 Hz and 12° amplitude. The results demonstrate non-monotonic dependence of thrust on stiffness setting ϕ.

For testing, the robot was adjusted to neutral buoyancy so that it remained just below the water surface. The pectoral

(a)

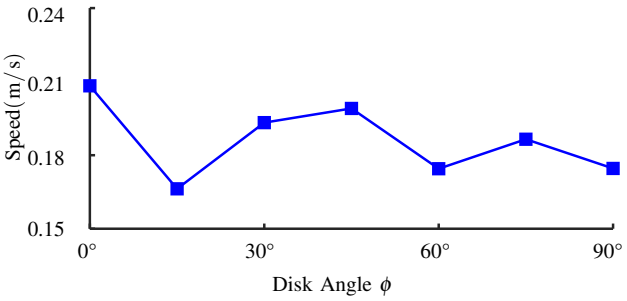

(b)

Fig. 9. Free swimming test. (a) Experimental pool setup with dimensions and camera placement. (b) Average swimming speed for underwater flapping at 0.667 Hz and 30° amplitude under different stiffness settings ϕ. Results show that swimming speed decreases as stiffness increases.

fins were actuated at a frequency of 0.667 Hz with a flapping amplitude of 30°. The resulting average swimming speeds for different stiffness configurations are presented in Fig. 9(b).

The results show that fin stiffness significantly affects swimming speed. Under low-frequency, large-amplitude flapping, average speed generally decreases as the disk setting ϕ increases from 0° to 90°. Notably, the swimming speed trends do not precisely match the thrust measurements. Two factors likely contribute to this discrepancy. First, the hydrodynamic conditions experienced by a freely moving robot differ from those of a fixed robot, with additional drag or thrust arising from body–fluid interactions. Second, environmental disturbances and the absence of closed-loop control may reduce swimming efficiency in some trials.

Overall, the free-swimming experiments provide system-level evidence that tunable fin stiffness influences locomotor performance, complementing and reinforcing the thrust test findings.

V. Conclusion

This work demonstrates the development and evaluation of a manta ray–inspired robot equipped with an active stiffness control mechanism for reconfigurable, two-dimensional stiffness distributions in its pectoral fins. By integrating a cable-driven actuation system with anisotropic disks, the robot achieves multiple distinct stiffness states that can be locked during operation, thereby overcoming the limitations of fixed or one-dimensional adjustable stiffness found in existing manta ray robots.

Mechanical characterization confirmed periodic stiffness variation, with spanwise stiffness increasing by more than 30% and chordwise stiffness decreasing by approximately 10% as the disk rotated from 0° to 90°, then recovering as it rotated from 90° to 180°. Robot experiments further quantified the hydrodynamic implications of stiffness tuning. Thrust tests revealed that stiffness substantially affects steady-state thrust generation, with the optimal stiffness setting producing up to five times more thrust than the least effective configuration. Free-swimming trials showed that stiffness adjustments influence swimming speed, with variations of up to 20% observed under low-frequency, large-amplitude flapping conditions.

Collectively, these findings highlight the significant role of structural compliance in aquatic locomotion and demonstrate that active stiffness control can enhance the performance and adaptability of bio-inspired underwater robots. Future work will focus on refining the actuation mechanism, implementing closed-loop control for real-time stiffness adjustment, and performing extended field trials to validate performance in dynamic aquatic environments. This research underscores the potential of stiffness tuning as a powerful design strategy for improving efficiency, maneuverability, and versatility in next-generation robotic swimmers.

REFERENCES

[1] F. E. Fish, "Advantages of aquatic animals as models for bio-inspired drones over present auv technology," *Bioinspiration & biomimetics*, vol. 15, no. 2, p. 025001, 2020.

[2] Q. Zhao, T. Yang, G. Tang, Y. Yang, F. Dong, Z. Xi, Y. Zou, M. Xu, S. Li, C. Wang, and G. Xie, "Bio-inspired swarm of underwater robots: a review," *Bioinspiration & Biomimetics*, vol. 20, no. 041002.

[3] Y. Zhai, X. Zheng, L.-M. Chao, S. Li, M. Xiong, Y. Jia, L. Li, and G. Xie, "An interpretable approach to estimate the self-motion in fish-like robots using mode decomposition analysis," *Nature Communications*, vol. 16, no. 1, p. 3887, 2025.

[4] Y. Chen, T. Wang, C. Wu, and X. Wang, "Design, control, and experiments of a fluidic soft robotic eel," *Smart Materials and Structures*, vol. 30, no. 6, p. 065001, 2021.

[5] R. Hall, G. Espinosa, S.-S. Chiang, and C. D. Onal, "Design and testing of a multi-module, tetherless, soft robotic eel," in *2024 IEEE International Conference on Robotics and Automation (ICRA)*. IEEE, 2024, pp. 8821–8827.

[6] K. Struebig, B. Bayat, P. Eckert, A. Looijestijn, T. C. Lueth, and A. J. Ijspeert, "Design and development of the efficient anguilliform swimming robot—mar," *Bioinspiration & Biomimetics*, vol. 15, no. 3, p. 035001, 2020.

[7] J. Zhu, C. White, D. K. Wainwright, V. Di Santo, G. V. Lauder, and H. Bart-Smith, "Tuna robotics: A high-frequency experimental platform exploring the performance space of swimming fishes," *Science Robotics*, vol. 4, no. 34, p. eaax4615, 2019.

[8] H. Godaba, J. Li, Y. Wang, and J. Zhu, "A soft jellyfish robot driven by a dielectric elastomer actuator," *IEEE Robotics and Automation Letters*, vol. 1, no. 2, pp. 624–631, 2016.

[9] S.-W. Yeom and I.-K. Oh, "A biomimetic jellyfish robot based on ionic polymer metal composite actuators," *Smart materials and structures*, vol. 18, no. 8, p. 085002, 2009.

[10] L. J. Rosenberger, "Pectoral fin locomotion in batoid fishes: undulation versus oscillation," *Journal of Experimental Biology*, vol. 204, no. 2, pp. 379–394, 2001.

[11] F. E. Fish, A. Kolpas, A. Crossett, M. A. Dudas, K. W. Moored, and H. Bart-Smith, "Kinematics of swimming of the manta ray: three-dimensional analysis of open-water maneuverability," *Journal of Experimental Biology*, vol. 221, no. 6, p. jeb166041, 2018.

[12] Y. Cai, S. Bi, G. Li, H. P. Hildre, and H. Zhang, "From natural complexity to biomimetic simplification: The realization of bionic fish inspired by the cownose ray," *IEEE Robotics & Automation Magazine*, vol. 26, no. 3, pp. 27–38, 2018.

[13] J. Li, W. Li, Q. Liu, B. Luo, and W. Cui, "Current status and technical challenges in the development of biomimetic robotic fish-type submersible," *Ocean-Land-Atmosphere Research*, vol. 3, p. 0036, 2024.

[14] A. Prakash, A. R. Nair, H. Arunav, R. P R, V. M. Akhil, C. Tawk, and K. V. Shankar, "Bioinspiration and biomimetics in marine robotics: a review on current applications and future trends," *Bioinspiration & Biomimetics*, vol. 19, no. 3, p. 031002, apr 2024. [Online]. Available: https://dx.doi.org/10.1088/1748-3190/ad3265

[15] S. A. Hasib, M. M. Gulzar, S. R. Oishy, M. Maaruf, S. Habib, and A. Shakoor, "An investigation of innovative strategies in underwater soft robotics," *Engineering Science and Technology, an International Journal*, vol. 70, p. 102123, 2025.

[16] B. Lu, C. Zhou, J. Wang, Z. Zhang, and M. Tan, "Toward swimming speed optimization of a multi-flexible robotic fish with low cost of transport," *IEEE Transactions on Automation Science and Engineering*, vol. 21, no. 3, pp. 2804–2815, 2024.

[17] R. Russo, S. Blemker, F. Fish, and H. Bart-Smith, "Biomechanical model of batoid (skates and rays) pectoral fins predicts the influence of skeletal structure on fin kinematics: implications for bio-inspired design," *Bioinspiration & biomimetics*, vol. 10, no. 4, p. 046002, 2015.

[18] Y. Cao, T. Bao, Y. Cao, P. Wang, O. Yang, Y. Lu, and Y. Cao, "Effects of bionic bone flexibility on the hydrodynamics of pectoral fins," *Journal of Marine Science and Engineering*, vol. 10, no. 7, p. 981, 2022.

[19] D. Quinn and G. Lauder, "Tunable stiffness in fish robotics: mechanisms and advantages," *Bioinspiration & Biomimetics*, vol. 17, no. 1, p. 011002, 2021.

[20] Y. Xiang, L. Gu, K. Ye, Z. Zhang, Z. Gong, and B. Tao, "The foldable fin with dynamic adjustments for manta ray-inspired robots," *IEEE Robotics and Automation Letters*, 2025.

[21] ——, "A variable stiffness fin for manta ray-inspired robots with two motion modals," *IEEE Robotics and Automation Letters*, 2025.

[22] K. C. Hall, P. J. Hundt, J. D. Swenson, A. P. Summers, and K. D. Crow, "The evolution of underwater flight: the redistribution of pectoral fin rays, in manta rays and their relatives (myliobatidae)," *Journal of morphology*, vol. 279, no. 8, pp. 1155–1170, 2018.

[23] M. E. Hagood, J. R. Alexander, S. Kajiura, and M. E. Porter, "Batoid skin mechanical properties and morphology vary among functional swimming styles," *Acta Biomaterialia*, 2025.

[24] L. J. Rosenberger and M. W. Westneat, "Functional morphology of undulatory pectoral fin locomotion in the stingray taeniura lymma (chondrichthyes: Dasyatidae)," *Journal of Experimental Biology*, vol. 202, no. 24, pp. 3523–3539, 1999.

[25] Y. Li, Y. Xu, Z. Wu, L. Ma, M. Guo, Z. Li, and Y. Li, "A comprehensive review on fish-inspired robots," *International Journal of Advanced Robotic Systems*, vol. 19, no. 3, p. 17298806221103707, 2022.

[26] C. Zhou and K.-H. Low, "Better endurance and load capacity: an improved design of manta ray robot (roman-ii)," *Journal of Bionic Engineering*, vol. 7, pp. S137–S144, 2010.

[27] Y. Cai, L. Chen, S. Bi, G. Li, and H. Zhang, "Bionic flapping pectoral fin with controllable spatial deformation," *Journal of Bionic Engineering*, vol. 16, no. 5, pp. 916–930, 2019.

[28] C.-M. Chew, Q.-Y. Lim, and K. S. Yeo, "Development of propulsion mechanism for robot manta ray," in *2015 IEEE International Conference on Robotics and Biomimetics (ROBIO)*, 2015, pp. 1918–1923.

[29] L. Chen, S. Bi, Y. Cai, Y. Cao, and G. Pan, "Design and experimental research on a bionic robot fish with tri-dimensional soft pectoral fins inspired by cownose ray," *Journal of Marine Science and Engineering*, vol. 10, no. 4, p. 537, 2022.